TWO-PHASE FLOW COMPUTATIONS BY THE HYBRID PARTICLE-LEVEL-SET METHOD

Daniel Gaudlitz and Nikolaus A. Adams
Lehrstuhl für Aerodynamik,
Technische Universität München
Boltzmannstr. 15, D-85748 Garching, Germany
daniel.gaudlitz@aer.mw.tum.de

ABSTRACT

In the present paper we investigate two-phase flows by numerical simulations with the hybrid particle-level-set method (HPLS). The HPLS-scheme is an extension of the original level-set technique with the purpose of improving mass conservation for moving interfaces. We have applied the HPLS-method to the simulation of gas bubbles rising in liquids. These two-phase flows exhibit large density and viscosity ratios, and a significant surface-tension force acts at the interface. Flow configurations with steadily rising bubbles with a closed wake and bubbles with open wakes ascending on spiraling paths have been investigated. The former were used mainly for validation purposes by confirming that the geometry of the closed wake is in good agreement with experiments. For the latter configuration the open unsteady wake leads to a helical or a zig-zag ascent path. It is confirmed that a periodic shedding of large vortical structures accompanies the lateral movement of the bubble.

INTRODUCTION

For many technical applications the numerical simulation of incompressible two-phase flows with large density differences is important. Examples can be found in metallurgy, where the injection of gas bubbles in a melt is used for stirring and alloying processes. Often flow parameters are such that complex interface deformations have to be expected.

In our numerical simulations of two-phase flows we use the hybrid particle-level-set method proposed by Enright et al. (2002) for modeling the phase boundary. The method combines the level-set scheme with an interface tracking by marker particles. Since their introduction by Osher and Sethian (1988) level-set schemes have been subject to further development and improvement (Osher and Fedkiw 2001, Sethian and Smereka 2003) and are nowadays an important alternative to volume-of-fluid or particle-tracking approaches. With level-set methods formally no reconstruction of the interface is necessary and the computation of quantities at the interface, e.g., the local curvature and the unit normal vector is straightforward due to the continuous definition of the level-set function. However, in regions of large curvature the interface might become marginally resolved by the underlying computational mesh, leading to mass losses in these areas. The hybrid particle-level-set method uses marker particles to correct mass errors in the level-set representation of the interface. Lagrangian marker-particle schemes preserve mass of the phases exactly but the continuous reconstruction of interfaces is difficult, in particular for cases with interfaces merging or breaking up. With the HPLS-method two sets of massless marker particles are seeded in the vicinity of the interface and this particle distribution is used to track the phase boundary throughout the simulation. Whenever there is a disagreement between the interface representation given by the level-set function and the marker-particle positions the level-set function is corrected.

The improvement by the HPLS-scheme with respect to efficiency and accuracy compared to a pure level-set approaches has been shown by Enright et al. (2002) and by Gaudlitz and Adams (2004) for generic numerical test cases. In this paper we apply the method to two-phase flows characterized by large density ratios and involving surface-tension forces. After giving the basic mathematical equations of the method we review their numerical discretization. We will discuss results of direct numerical simulations of gas bubbles rising in liquids showing linear or zig-zag ascent paths.

MATHEMATICAL FORMULATION

The governing equations for the fluid velocity $\underline{u}$ and pressure p for incompressible two-phase flows are given by

$$\begin{aligned} \underline{u}_t + \underline{u}\cdot\nabla\underline{u} &= -\frac{\nabla p}{\rho} + \frac{1}{Re_{ref}\cdot\rho}\nabla\cdot(2\mu\mathbf{D}) + \\ &\quad + \frac{\underline{g}_u}{Fr_{ref}^2} - \frac{1}{We_{ref}\cdot\rho}\kappa\delta\underline{N}\,, \qquad (1) \\ \nabla\cdot\underline{u} &= 0\,. \qquad (2) \end{aligned}$$

Herein ρ and μ are the local density and viscosity, respectively, $\mathbf{D}$ is the rate-of-deformation tensor, whose components are $D_{ij} = \frac{1}{2}(u_{i,j} + u_{j,i})$ and $\underline{g}_u$ is the unit gravity vector. κ denotes the curvature of the phase interface, δ is a delta function being zero everywhere except near the interface, and $\underline{N}$ is the unit normal vector at the interface.

The above equations are non-dimensionalized leading to the following parameters:

$$\begin{aligned} Re_{ref} &= \frac{\rho_c L U}{\mu_c} \quad \text{reference-Reynolds number,} \\ Fr_{ref} &= \frac{U}{\sqrt{gL}} \quad \text{reference-Froude number,} \\ We_{ref} &= \frac{\rho_c L U^2}{\sigma} \quad \text{reference-Weber number,} \end{aligned}$$

where ρ_c is the density and μ_c is the dynamic viscosity of the continuous phase. L is a reference length, U a reference velocity and σ is the surface-tension coefficient.

The two phases are distinguished by the level-set function. The interface between the two immiscible phases is given by the zero level-set of a scalar function $\phi(\underline{x}, t)$. Away

from the interface the level-set function ϕ gives the signed distance to the interface, being negative in the gas phase and positive in the liquid phase.
Density and viscosity are computed by Eqs. (3) and (4), where the subscripts 'c' and 'd' correspond to the two different phases,

$$\rho(\phi) = \rho_d + (\rho_c - \rho_d) \cdot H(\phi), \tag{3}$$

$$\mu(\phi) = \mu_d + (\mu_c - \mu_d) \cdot H(\phi). \tag{4}$$

$H(\phi)$ is a Heaviside function mollified within a small region ϵ on each side of the interface

$$H(\phi) = \begin{cases} 0 & , \text{if } \phi < -\epsilon \\ \frac{1}{2}(1 + \frac{\phi}{\epsilon} + \frac{1}{\pi}\sin(\frac{\pi\phi}{\epsilon})) & , \text{if } -\epsilon \leq \phi \leq \epsilon \\ 1 & , \text{if } \phi > \epsilon. \end{cases} \tag{5}$$

The level-set function is advected by the local flow velocity

$$\phi_t + \underline{u} \cdot \nabla\phi = 0. \tag{6}$$

While Eq. (6) transports the zero level-set, i.e. the interface, the signed-distance property is lost in general. However, for the computation of the surface-tension term involving curvature and the normal vector as well as for the smoothing of variables near the interface it is essential to maintain ϕ as a distance function. To reestablish the signed-distance property a reinitialization procedure by solving Eq. (7) to steady state has to be carried out after each time step

$$\phi_\tau + \text{sign}\,(\phi) \cdot (|\nabla\phi| - 1) = 0. \tag{7}$$

Besides the level-set function describing the phase boundary, the HPLS-method places two sets of massless marker particles near the interface. Positive particles are assigned to $\phi > 0$ and negative particles to $\phi < 0$. The particle evolution in time is given by

$$\frac{d\underline{x}_P}{dt} = \underline{u}(\underline{x}_P). \tag{8}$$

NUMERICAL METHOD

For the discretization of the above equations we use finite differences on an equidistant staggered grid. Incompressibility is enforced by a fractional step projection method. First, the right-hand side composed by convection, dissipation, buoyancy and surface-tension terms is computed and evolved forward in time, Eq. (9), giving an intermediate velocity $\underline{u}^*$. The Poisson equation for the pressure, Eq. (10), is solved and the intermediate velocity $\underline{u}^*$ is made divergence free resulting in the velocity field $\underline{u}^{n+1}$ at the next time step, Eq. (11).

$$\frac{\underline{u}^* - \underline{u}^n}{\delta t} = -(\underline{u}^n \cdot \nabla)\underline{u}^n + \frac{1}{\rho}\left(\frac{1}{Re_{ref}}\nabla \cdot (2\mu\mathbf{D}) + \right. \\ \left. + \frac{\underline{g}_u}{Fr^2_{ref}} - \frac{1}{We_{ref}}\kappa(\phi) \cdot \delta\,(\phi)\,\underline{N}(\phi)\right) \tag{9}$$

$$\nabla \cdot \left(\frac{1}{\rho}\nabla p\right) = \nabla \cdot \underline{u}^* \tag{10}$$

$$\underline{u}^{n+1} = \underline{u}^* - \frac{1}{\rho}\nabla p \tag{11}$$

The convective terms in the Navier-Stokes equations are discretized by fourth-order finite differences (Morinishi, 1998) which simultaneously conserve mass, momentum and kinetic energy on uniform staggered grids. Viscous terms are discretized by second-order finite differences. When computing flows with fluid interfaces the surface-tension force acting at phase boundaries has to be taken into account. This additional source term is given by the last term on the right-hand side of Eq. (9) and includes the unit normal vector at the interface

$$\underline{N}(\phi) = \frac{\nabla\phi}{|\nabla\phi|}\ , \tag{12}$$

and the curvature of the interface

$$\kappa(\phi) = \nabla \cdot \left(\frac{\nabla\phi}{|\nabla\phi|}\right)\ . \tag{13}$$

Spatial derivatives in Eqs. (12) and (13) are computed by second-order central differences. With the continuum-surface-force approach (Brackbill, 1992) a mollified delta function

$$\delta(\phi) = \begin{cases} \frac{1}{2\epsilon}\left(1 + \cos\left(\frac{\pi\phi}{\epsilon}\right)\right) & , \text{if } |\phi| < \epsilon \\ 0 & , \text{otherwise,} \end{cases} \tag{14}$$

is used to smooth the singular surface-tension force at the phase boundary. A detailed analysis of different implementations of the surface-tension term can be found in Gaudlitz and Adams (2006).
The Poisson equation, Eq.(10), is discretized by second-order finite differences and the resulting system of quasi-linear equations is solved by a preconditioned conjugate-gradient method. For evolution in time of the Navier-Stokes equations, Eq. (1), the level-set function, Eq. (6), and the particle positions, Eq. (8), a third-order Runge-Kutta scheme is employed.

The procedure for evolving interfaces in time with the HPLS-method is as follows: First, the level-set function, Eq. (6), and the particle positions, Eq. (8), are evolved forward in time. Spatial derivatives in Eq. (6) are computed by a high-order WENO-scheme and in Eq. (8) the particle velocities $\underline{u}(\underline{x}_P)$ are interpolated linearly.
Second, the level-set function needs to be reinitialized by solving Eq. (7), where again a high-order WENO-scheme for the spatial derivatives and a Runge-Kutta scheme for integration in time is used. The sign function in Eq. (7) is defined as

$$\text{sign}(\phi) = \frac{\phi}{\sqrt{\phi^2 + h^2}}, \tag{15}$$

where smoothing over a single cell width h is incorporated. For sufficiently small time steps ϕ does not differ too much from a distance function and therefore Eq. (7) needs to be evolved for a few steps in pseudo-time τ only.
Finally, a correction of the level-set function by the marker particles is carried out in order to improve mass conservation properties of the scheme. Although formally Eq. (7) does not alter the location of the zero level-set this is not the case for the discrete approximation. In Gaudlitz and Adams (2006) the reinitialization step has been identified to cause a major contribution to the mass loss during simulations. Instead of performing a particle correction after level-set transport and after reinitialization (Enright et al. 2002) we perform the particle correction only once per time step after the reinitialization.

In the following we give an overview of the particle correction algorithm. Positive and negative particles are seeded at the corresponding sides of the interface described by $\phi = 0$. At each time step a radius r_P which is bounded

by a lower and upper limit depending on the resolution of the computational grid is assigned to each particle. With $r_{min} = 0.1 \cdot h$ and $r_{max} = 0.5 \cdot h$ the radii of the particles are set as

$$r_P = \begin{cases} r_{max} & \text{, if } \text{sign}_\text{P}\, \phi(\underline{x}_P) > r_{max} \\ \text{sign}_\text{P}\, \phi(\underline{x}_P) & \text{, if } r_{min} \leq \text{sign}_\text{P}\, \phi(\underline{x}_P) \leq r_{max} \\ r_{min} & \text{, if } \text{sign}_\text{P}\, \phi(\underline{x}_P) < r_{min}, \end{cases} \tag{16}$$

where sign_P indicates wether the particle belongs to phase $\phi > 0 \Rightarrow \text{sign}_\text{P} = +1$ or to phase $\phi < 0 \Rightarrow \text{sign}_\text{P} = -1$. After performing the reinitialization step all particles are detected, which have crossed the interface $\phi = 0$ by a distance of more than their radius. These 'escaped' particles are associated with a spherical level-set function

$$\phi_P(\underline{x}) = \text{sign}_\text{P}\left(r_P - |\underline{x} - \underline{x}_P|\right), \tag{17}$$

where the particle radius r_P describes the zero level-set $\phi_P(\underline{x}) = 0$ of this function. Equation (17) is evaluated at the eight corners of the cell containing the particle. If ϕ_P differs from the level-set function ϕ at these locations the interface $\phi = 0$ requires correction.
The set of escaped positive particles E^+ is used to reconstruct the $\phi > 0$ region and the escaped negative particles E^- are used to reconstruct the $\phi < 0$ region. The corrected local level-set value is obtained by choosing either ϕ^+ or ϕ^- whichever is smallest in magnitude

$$\phi = \begin{cases} \phi^+ & \text{, if } |\phi^+| \leq |\phi^-| \\ \phi^- & \text{, if } |\phi^+| > |\phi^-|, \end{cases} \tag{18}$$

where

$$\phi^+ = \max_{p \in E^+} (\phi_P, \phi) \quad \text{, and}$$
$$\phi^- = \min_{p \in E^-} (\phi_P, \phi)\ .$$

RESULTS OF SIMULATIONS

Bubbles with closed wake

A detailed experimental investigation of air bubbles rising in a water-glucose solution has been done by Bhaga and Weber (1981). By using different glucose concentrations the dynamic viscosity of the liquid was varied while the liquid density and the surface-tension coefficient remained nearly unaffected. The Morton number $Mo = (g \cdot \mu_c^4)/(\rho_c \cdot \sigma^3)$ ranges from 850 to $7,4 \cdot 10^{-4}$. Air bubbles of equal volume were found to develop very different shapes depending on the Morton number. At high Morton numbers the flow is strongly influenced by viscous forces and the bubbles remain almost spherical or become slightly ellipsoidal. For smaller Morton numbers the bubble shape changes to a flat axisymmetric cap.

We have performed numerical simulations of single bubbles at two different Morton numbers. In table 1 the parameters of the simulations are summarized, where d_B is the initial bubble diameter, X, Y, Z are the spatial extends of the cartesian domain, and N_x, N_y, N_z are the number of cells in the three coordinate directions. In order to properly resolve the high curvature at the outer region of the cap-type bubble a finer grid had to be used for *Case 2*. The liquid and the gas phase were initially at rest and a spherical bubble was initialized at the center of the computational domain.

After an initial transient the bubble shape and its wake reach a stationary state. The measured terminal rising velocities U_T and the bubble-Reynolds number $Re_B = U_T \cdot d_B \cdot \rho_c/\mu_c$ are summarized in table 2. An empirical estimate for the terminal rising velocity has been given by Angelino (1966). This prediction is based only on the Morton number characterizing the gas-liquid system and the bubble volume V and gives remarkably good results when compared with our simulation data. The units of V and U_T in Eq. (19) are cm^3 and cm/s, respectively.

$$U_T = KV^m \tag{19}$$
$$K = \frac{25}{1 + 0.33Mo^{0.29}}$$
$$m = \frac{0.167}{1 + 0.34Mo^{0.24}}$$

Figures 1 and 2 show a comparison of the stationary bubble shapes between experiments and simulation. In *Case 1* the bubble developes an oblate ellipsoidal shape with an

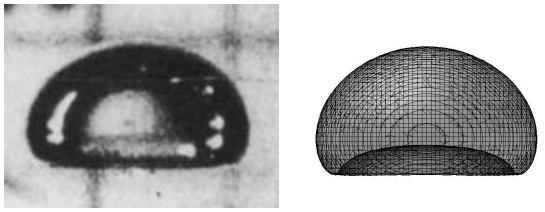

(a) Experiment (b) Numerical simulation

Figure 1: Bubble shapes for *Case 1*.

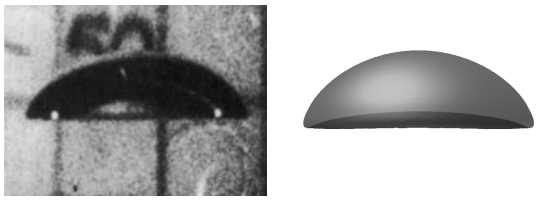

(a) Experiment (b) Numerical simulation

Figure 2: Bubble shapes for *Case 2*.

Table 1: Parameters of the simulation.

	Case 1	*Case 2*
Mo	41.1	0.103
Re_{ref}	13.91	62.03
We_{ref}	116	116
Fr_{ref}	1.0	1.0
ρ_d/ρ_c	1/1070	1/1048
μ_d/μ_c	1/71978	1/15824
$X \times Y \times Z$	$4\,d_B \times 8\,d_B \times 4\,d_B$	
$N_x \times N_y \times N_z$	160×320×160	240×480×240

Table 2: Terminal rising velocities and bubble-Reynolds number.

	Case 1		*Case 2*	
	U_T (m/s)	Re_B	U_T (m/s)	Re_B
Experiment	0.26	7.2	0.34	42.2
Simulation	0.25	6.9	0.33	40.2
Angelino (1966)	0.25	-	0.33	-

indentation at its lower side. For *Case 2* this indentation develops further towards a cap-type shape as the final stationary state. A comparison of characteristic parameters of the bubble geometries in Fig. 3 reveals a good agreement of the experimental and numerical results. In Fig. 3(d) bubble drag coefficients of experiments and simulations are shown, where in the simulations c_D has been computed from

$$c_D = \frac{4 \cdot g \cdot d_B}{3 \cdot U_T^2} \tag{20}$$

In the literature various empirical correlations for determining the drag coefficient can be found. However, their validity is restricted to specific bubble shapes or limited ranges of Reynolds numbers mostly. The drag law given by Mei et al. (1994) takes into account the existence of a bubble wake as well as that of a shear layer at the bubble surface, but it is valid only for almost spherical bubbles. Hence the values predicted by this correlation differ from the experimental and our numerical results for $Re_B > 5$, where ellipsoidal and cap-type bubbles develop at the considered Morton numbers. Similarly, the correlation $c_D = 14.9/Re^{0.78}$ proposed by Clift et al. (1978) gives reasonable values for the drag coefficient for nearly spherical bubbles only. A very good agreement of the experimental and numerical results is obtained with the empirical relation $c_D = (16/Re)+2$ of Taylor and Acrivos (1964), see Fig. 3(d).
Due to the high viscosity of the liquid the Reynolds numbers are relatively small leading to closed laminar wakes. Width and length of the wakes are shown in Figs. 4(a) and 4(b), respectively, where a good agreement between experiment and simulation is obtained. The same is found for the parameter h_S, Fig. 3(a), describing the wake structure, see Fig. 4(c).

Bubbles with open wake

In numerous experiments of air bubbles rising in water linear ascent paths have been observed for bubble diameters less than $1.2\,mm$. For larger diameters the bubble rises unsteadily on spiral or zig-zag paths. For the investigation of an air bubble with $d_B = 4\,mm$ rising in water on a zig-zag path the following parameters have been chosen: the reference-Reynolds number is $Re_{ref} = 269$, the reference-Weber number is $We_{ref} = 2.15$, and the reference-Froude number is $Fr_{ref} = 1.0$. The density ratio for air bubbles rising in water is $\rho_d/\rho_c = 1/774$ and the ratio of the dynamic viscosities is $\mu_d/\mu_c = 1/54$. Periodic boundary conditions have been used for the computational domain with the extents $X = 4\,d_B, Y = 8\,d_B$ and $Z = 4\,d_B$. The number of grid cells along the coordinate axes are $N_x = 70, N_y = 140$ and $N_z = 70$. As this grid resolution was found not to resolve the smallest flow scales the reference-Reynolds number was reduced in a second attempt to $Re_{ref} = 269$. The simulation was initialized with a spherical bubble at rest.

During the initial phase the bubble deforms to an oblate ellipsoid with a mean ratio of the major horizontal axis to the vertical axis of 2.15. We note, that with onset of a zig-zag path also the bubble shape starts to oscillate periodically. In Fig. 5(a) the zig-zag path of the center-of-gravity of the bubble during rise is shown. For this particular simulation the plane containing the zig-zag motion is oriented approximately along the diagonal of the X-Z plane. This orientation is a random consequence of round-off errors since other orientations were observed for other simulations. We measured an oscillation frequency of $6.8\,Hz$ and an amplitude of $r_{amp} = 0.72\,d_B$.

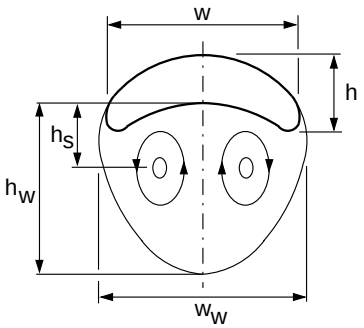

(a) Definition of bubble and wake geometry.

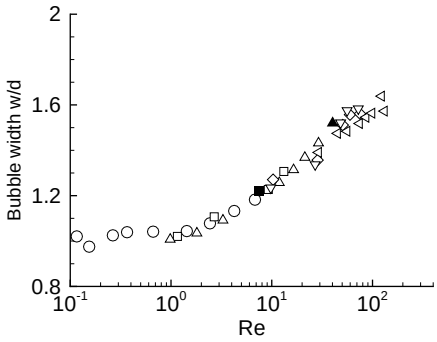

(b) Bubble width.

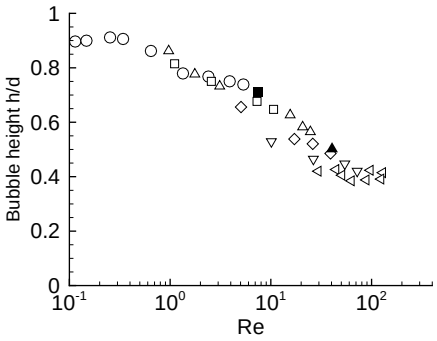

(c) Bubble height.

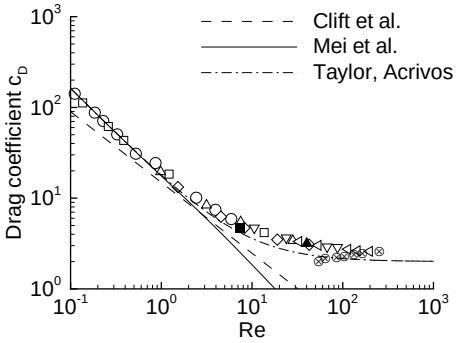

(d) Bubble drag coefficient.

Figure 3: Geometry and drag coefficient of the bubble. Morton numbers in the experiments are: ◯ : 711; □: 55.5; △: 4.17; ◇:1.03; ▽: 0.108; ◁: $5.48 \cdot 10^{-3}$; ⊗: $1.64 \cdot 10^{-3}$. Numerical simulations: ■: *Case 1*; ▲: *Case 2*.

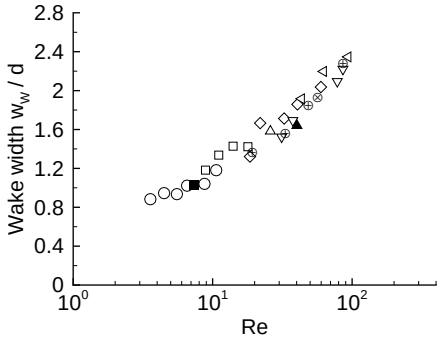

(a) Width of bubble wake.

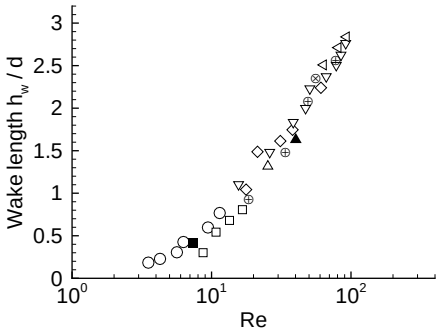

(b) Length of bubble wake.

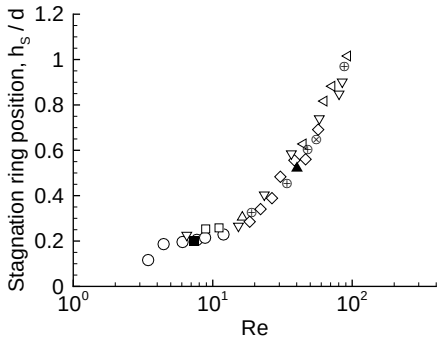

(c) Position of the wake stagnation ring.

Figure 4: Geometry of the wake. Morton numbers in the experiments are: ◯ : 258; □: 43.5; △: 4.41; ◇:0.962; ▽: 0.144; ◁: $4.58{\cdot}10^{-3}$; ⊗ : $1.73{\cdot}10^{-2}$; ⊕ : $6.5{\cdot}10^{-2}$. Numerical simulations: ■: *Case 1*; ▲: *Case 2*.

Figure 5(b) shows the bubble shape and the trailing vortex structures at an instant in time. We observe a quantitatively similar behaviour as in the experiments of Brücker (1999) of larger Reynolds number. Brücker identified a periodic shedding of hairpin-like vortical structures to accompany the zig-zag paths. Whenever the zig-zag motion reverses a hairpin-like vortex forms at the trailing edge of the bubble. In Fig. 5(b) the two vertically aligned legs of this flow structure are identified by two iso-contours of the streamwise vorticity ω_y, colored grey and black, which have the same magnitude but opposite signs.

The entire period of the zig-zag motion is spanned by six snapshots in X-Z planes, Fig. 7. The cross section of the bubble through its center-of-gravity is illustrated together with iso-contours of the streamwise vorticity ω_y in a horizontal plane a distance of $0.5\,d_B$ below the lower bubble surface. The arrow specifies the respective

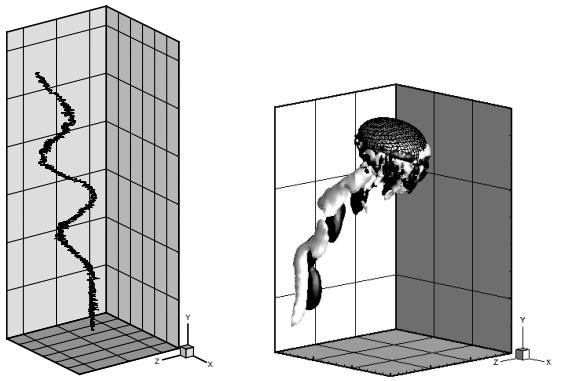

(a) 3D rising path. (b) Bubble surface and iso-contours of ω_y at an instant in time.

Figure 5: Bubble rising on a zig-zag path.

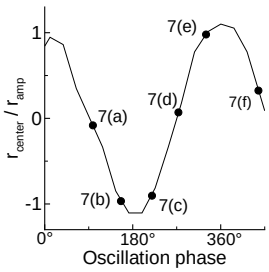

Figure 6: Motion of the center-of-gravity of the bubble.

direction of the lateral bubble motion and the arrow length is proportional to the lateral bubble velocity. For a better illustration of the phases of bubble motion shown in Fig.7 the respective position of the center-of-gravity of the bubble is highlighted in Fig. 6. Herein r_{center} is the distance between the center-of-gravity of the bubble and the center line of the zig-zag motion.

A counter-rotating vortex pair representing the two legs of the hairpin-like vortex can be clearly identified in Fig. 7(a). At this instant the bubble has just passed the 90° phase angle of the path oscillation, see Fig. 6, and the lateral velocity is now maximum. The hairpin-like vortex follows the bubble in its wake. Shortly before reaching the next reversing point at 180° phase angle a new pair of vortex legs is found, but now with opposite direction of rotation, see Fig 7(b). Figure 7(c) shows the bubble just after it has passed the 180° phase angle of its lateral motion. The new vortex legs have grown in strength, while the previous hairpin-like vortex is shed from the bubble and moves away. The bubble crosses 270° phase angle of the oscillation with the trailing vortex legs reaching their highest intensity, see Fig. 7(d). In Fig. 7(e) the bubble approaches the 360° phase angle, where the trailing hairpin-like vortex is shed and a new vortex developes at the opposite side of the bubble. At the bubble position shown in Fig. 7(f) one period is completed. Note that due to the periodic boundary conditions the trailing vortex system appears now at the bottom of Fig. 7(f).

Although the Reynolds number in this simulation is smaller than for the experiments of Brücker (1999) all flow phenomena leading to a zig-zagging rising path are captured. As found in experiments we also identified a periodic shedding of vortices from the bubble to accompany the observed zig-zag path.

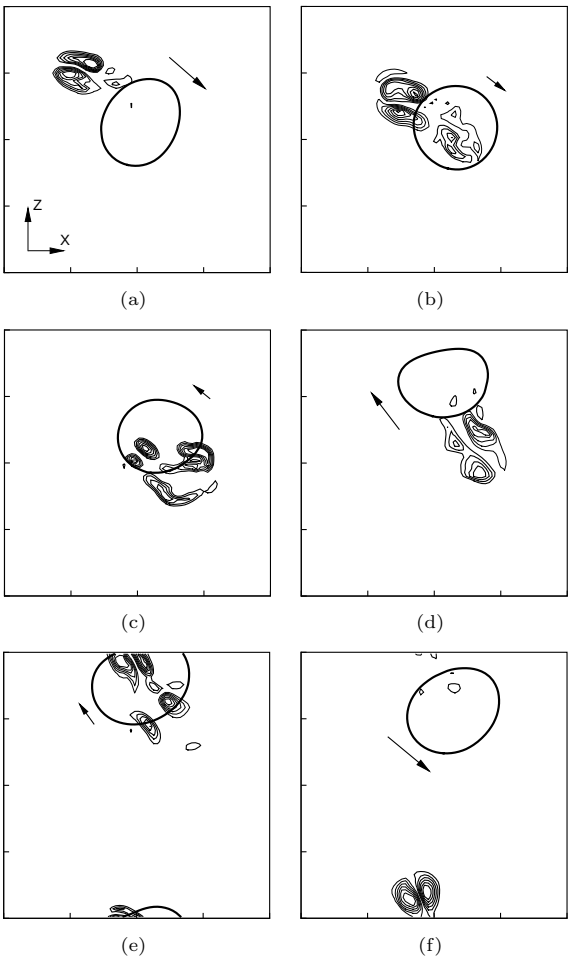

Figure 7: 2d bubble contours and streamwise vorticity in a horizontal plane in a distance of $0.5\,d_B$ below the lower bubble surface at different instants in time. Grey and thin black lines indicate negative and positive values of ω_y, respectively. The thick black line shows the instantaneous bubble contour.

CONCLUSIONS

The hybrid particle-level-set method has been employed to simulate gas bubbles rising in liquids. Such two-phase flows are characterized by large density and viscosity ratios and by the presence of surface-tension forces at the phase boundaries. For bubbles rising steadily on a linear path the bubble shape, the wake geometry and the terminal rising velocity obtained by numerical simulations have been found to be in excellent agreement with experimental data. For bubbles ascending on zig-zag paths we captured the mechanism of periodic vortex shedding related to this lateral bubble motion. In attempts to compute such flows with a pure level-set algorithm on grids refined by a factor of two the computational work increased significantly but the accuracy of the HPLS-scheme could not be reached.

REFERENCES

Angelino, H., 1966, "Hydrodynamique des grosses bulles dans les liquides visqueux", Chem. Eng. Sci., Vol. 21, pp. 541-550.

Bhaga, D., and Weber, M. E., 1981, "Bubbles in viscous liquids: shapes, wakes and velocites", J. Fluid Mech., Vol. 105, pp. 61-85.

Brackbill, J., Kothe, D., and Zemach, C., 1992, "A continuum method for modeling surface tension", J. Comput. Phys., Vol. 100, pp. 335-354.

Brücker, C., 1999, "Structure and dynamics of the wake of bubbles and its relevance for bubble interaction", Phys. Fluids, Vol. 11, pp. 1781-1796.

Clift, R. C., Grace, J. R., and Weber, M. E., 1978, *"Bubbles, Drops and Particles"*, Academic, New York

Enright, D., Fedkiw, R., Ferziger, J., and Mitchell, I., 2002, "A hybrid particle level set method for improved interface capturing", J. Comput. Phys., Vol. 183, pp. 83-116.

Gaudlitz, D., and Adams, N. A., 2004, "A hybrid particle-level-set method for two-phase flows", *Proceedings, 75. Jahrestagung der Gesellschaft für Angewandte Mathematik und Mechanik*, Proc. Appl. Math. Mech., pp. 506-507.

Gaudlitz, D., and Adams, N. A., 2006, "The hybrid particle-level-set method applied to two-phase flows", *Proceedings of FEDSM2006, Joint U.S.-European Fluids Engineering Summer Meeting*, ASME: FEDSM2006-98126.

Mei, R., Klausner, J. F., and Lawrence, C. J., 1994, "A note on the history force on a spherical bubble at finite reynolds number", Phys. Fluids, Vol. 6, pp. 418-420.

Osher, S., and Sethian, J.A., 1988, "Fronts propagating with curvature-dependent speed: Algorithms based on Hamilton-Jacobi formulations", J. Comput. Phys., Vol. 79, pp. 12-49.

Osher, S., and Fedkiw, R., 2001, "Level set methods: An overview and some recent results", J. Comput. Phys., Vol. 169, pp. 463-502.

Sethian, J., and Smereka, P., 2003, "Level set methods for fluid interfaces", Annu. Rev. Fluid Mech., Vol. 35, pp. 341-372.

Taylor, T. D., and Acrivos, A., 1964, "On the deformation and drag of a falling viscous drop at low reynolds number", J. Fluid Mech., Vol. 18, pp. 466-477.